J Mater Sci: Mater Electron **(2024) 35:796**

The output performance evaluations of multilayered piezoelectric nanogenerators based on the PVDF-HFP/PMN-35PT using various layer-by-layer assembly techniques

Levent Paralı[1,*]

[1] *Department of Electronics and Automation, Manisa Celal Bayar University, Manisa 45400, Turkey*

Received: 6 January 2024
Accepted: 7 April 2024
Published online: 17 April 2024

ABSTRACT

Multilayered Poly (vinylidene fluoride-co-hexafluoropropylene) (PVDF-HFP) and lead magnesium niobate lead titanate Pb ($Mg_{1/3}Nb_{2/3}$) O_3–$PbTiO_3$ (PMN-35PT) composition-based piezoelectric nanogenerators (PNGs) were fabricated as series, parallel, and combined series-parallel connections using various layer-by-layer assembly techniques. Supporting the theoretical approaches with experimental results shows that the fabricated four-layered PNG with parallel connections (4L-P) reached an open-circuit voltage of 0.4 V (V_{RMS}) and a maximum electrical power of 0.3 μW (P_{RMS}) by drawing a current (I_{RMS}) of 1.46 μA under a resistive load of 140.2 KΩ. Increasing the capacitance and decreasing the impedance with the fabrication of the four-layer PNG by connecting the layers in parallel connection with the support of the impedance matching process led to an increase in electrical output. With the use of an impedance matching system, the piezoelectric performance tests revealed that the 4L-P-based PNG had a 6.7 times greater electrical power efficiency (72.92 μW) at the vibrational frequency of 20 Hz compared to that of the single-layered PNG (10.82 μW). Furthermore, the multilayer PNG was successfully used as a wearable sensor for the monitoring of human body motions in real time on an IOT (Internet of Things) platform.

1 Introduction

In recent years, the use of waste electricity obtained from clean and inexhaustible energy sources such as wind, vibration, magnetic, solar, and heat has attracted significant interest when considering additional power supplies for a new generation of wearable and portable electronic devices [1–4]. Mechanical vibrational energy that exists in the environment can be harvested by sensors using the piezoelectric direct effect [5]. In particular, in order to fabricate piezoelectric nanogenerators used in electric energy harvesting from biological activities, such as finger tapping, fist beating, foot stamping, and arm and wrist bending, smart piezoelectric polymers and ceramic materials can be deployed [6].

Address correspondence to E-mail: levent.parali@cbu.edu.tr

https://doi.org/10.1007/s10854-024-12557-w

Among the smart piezoelectric polymers, polyvinylidene fluoride (PVDF) and its derivatives like polyvinylidene fluoride-trifluoroethylene (PVDF-TrFE) and polyvinylidene fluoride-hexafluoropropylene (PVDF-HFP) have α, β, γ, δ, and ε crystalline phases that are derived through different processing conditions. The β and γ polar versions of these polymers are extensively used in some device fabrications, such as sensors, actuators, batteries, and energy harvesting systems [7]. Furthermore, the PVDF-HFP has superior qualities such as higher solubility, good biocompatibility, large optical transparency, a wide response range, better mechanical strength, and a well-aligned form compared to the PVDF [8–12]. However, since the smart polymers have much lower piezoelectric coefficients compared to perovskite ceramics [13], the new flexible composites were obtained by combining them with piezoelectric perovskite ceramics ($BaTiO_3$, PZT (Pb ($Zr_xTi_{(1-x)}$) O_3), PMN-PT (Pb ($Mg_{1/3}Nb_{2/3}$) O_3–$PbTiO_3$), ZnO, etc.) which have higher piezoelectric values, mechanical properties, and minimum dielectric losses [14–17]. Moreover, the hybrid (polymer + ceramic)-based electrospun composites produced by electrospinning display both micro- and nano-characteristics owing to the fact that their fibers have been aligned in the same direction [18, 19].

The dielectric constant values of electrospun composites based on the piezoelectric nanogenerators (PNGs) are distinctly lower than those of the solid PVDF polymers due to the high porosity of the electrospun fibers which includes a large void. This is due to the fact that the fiber webs can be viewed as multiphase materials comprised of three phases: polymer, ceramic particles, and an air fraction or a large void [20]. According to the literature, measurements of the changes in the effective output voltages associated with the PNG (single layered) were observed at approximately 150–200 mV [21–23]. The low conductivity of the polymer fibers obtained through the electrospinning method causes residual charges to accumulate on the fiber surfaces, and the PNGs produce low output voltages [24]. Consequently, due to a reduction in the adhesion between the fibers, electrospun composites constitute a loose structure. This large-scale loose structure causes the formation of inferior electrospun resilience and low-density fibers. Afterward, when this electrospun mat is exposed to external pressure, it faces a more general warping except for the fiber deformation, which determines the PNG's voltage.

Recently, therefore, many researchers have focused on building multilayer piezoelectric electrospun mats for high-performance PNGs [25, 26]. Zhang et al. demonstrated that the PZT ceramics with parallel connection possessed higher piezoelectric performance versatility than the PZT ceramics with series connection [27]. Young Won Kim et al. aimed to improve a PNG's output performance using multiplayer PVDF-TrFE electrospun mats and microbead-based electrodes together. They concluded that the microbead formation that was placed in the electrode could explain the boost in the output performances [28]. Ramisa Yahyapour and colleagues worked on a multilayered hybrid structure using electrospun nanofibers, and in order to improve the stress/strain distribution across the piezoelectric film, three different passive layer materials (aluminum, cellulose, and polyester) were used. This research concluded that the addition of aluminum, cellulose, and polyester could increase the electrical output by approximately 4.7, 3, and 4.2 times more, respectively, than the sample without a passive layer [29]. Xiangxin Du et al. focused on multilayered piezoelectric composites with a porous structure based on the PVDF/PZT obtained via a laminating method. They claimed that the PNG based on PVDF/10-wt.% PZT composite fibers, which has a 220 μm film thickness, has the output voltage and power 3.4 and 6.5 times greater than that of the PVDF/10-wt.% PZT casting film-based PNG [25].

On the other hand, despite the extensive research into piezoelectric PVDF nanofiber membranes, inconclusive electrical voltage outputs have often been reported. In some papers, the reported voltages varied by tens of volts. Such a large inconsistency was due to different test methods and voltmeters having different internal resistance [30]. These test results confirm that the internal resistance of the voltmeter can have a profound effect on the measured value of the output voltage. As the internal resistance of the voltmeter increased, the peak also voltage increased [31]. For example, when the internal resistance of a voltmeter was increased from 1 MΩ to 1 GΩ, the difference in the output voltage of the PNG was more than 130 times in constant contact mode (piezoelectric effect) and more than 90 times in contact separation mode (triboelectric effect) [30]. While an ideal voltmeter should have infinite resistance when measuring the open-circuit voltage of

a PNG, in reality, commercial voltmeters have an internal resistance of between 1 MΩ and 10 MΩ. In order to be able to make comparative assessments of the experiments conducted in the scientific literature, the measurement results must be compatible with the actual measurement results obtained using commercial voltmeters.

In this study, flexible electrospun based on the PVDF-HFP and the PVDF-HFP/%30vol.PMN-35PT was first prepared using the electrospinning method. In order to define the morphological and structural properties of the two samples, X-ray diffraction (XRD), Fourier transform infrared spectroscopy (FTIR), and scanning electron microscopy (SEM) analyses were performed. The thin PNG devices were then fabricated by placing single and multilayered electrospun mats based on the PVDF-HFP/%30vol.PMN-35PT between two aluminum electrode sheets. In order to obtain the multilayered structures based on the PVDF-HFP/%30vol.PMN-35PT using different layer-by-layer assembly techniques, such as series, parallel, and combined series-parallel connections, these mats were layered and compressed together using a pressing process. The main objective of this study is to evaluate the composite structures created by considering both the number of layers and the different layer connection shapes. Finally, the output performances such as voltage, current, and power of the multilayered PNG devices on the piezoelectric energy harvesting system were investigated and compared with a single-layered PNG.

2 Material and methods

2.1 Materials

The Poly (vinylidene fluoride-co-hexafluoropropylene) (PVDF-HFP) (molecular weight: 400.000 g/mol, Aldrich) was chosen as the host polymer, while N-dimethylformamide (DMF) (99.5%) and acetone (C3H6O, Merck) were used as solvents to disperse the PVDF-HFP. All of the chemicals used in the synthesis of the PMN-35PT powder were analytically pristine and were produced from the following sources: $(MgCO_3)_4$-Mg $(OH)_2$-$5H_2O$ (Sigma-Aldrich), TiO_2 (Evonik, Degussa P25), Nb_2O_5 (Alfa Aesar), and $(PbCO_3)_2$-Pb $(OH)_2$ (Alfa Aesar).

2.2 Methods

2.2.1 Synthesis of the PMN-35PT

The PMN-35PT-based powder was prepared by a conventional solid-state reaction technique, including the two-stage columbite precursor method, as explained in detail in our previous study [32]. The particle size of the PMN-35PT powder employed for the preparation of the PVDF-HFP/PMN-35PT-based nanofiber mats was in the range of ≤ 1 μm. The values of the piezoelectric coefficient − d_{33}, the dielectric constant (− ε_r), and the loss tangent (tanδ) at 10 kHz for the ceramic PMN-35PT have been measured as 530 pC/N, 3686, and 2.2%, respectively [32]. Being in the vicinity of the morphotropic pseudo-cubic phase boundary, these results agreed well with the PMN-35PT solid solutions [33–35].

2.2.2 Creation of the PVDF-HFP/PMN-35PT electrospun mats

Figure 1 shows in detail the construction of the PVDF-HFP/PMN-PT electrospun mat using the electrospinning process. The electrospinning system presented in Fig. 1a includes the following equipment: the programmable syringe pump (flow rate 2.0 mL/h), a rotating drum collector (length: 16 cm and diameter: 6 cm, and rotation speed: 2300 rpm), a plastic syringe (10 mL), a metal needle with a diameter of 0.4 mm, and a high-voltage DC (Direct Current) power supply.

All the electrospinning equipment is in a Plexiglass cabinet and the plastic syringe is positioned vertically on the pump. The plexiglass cabinet door is fitted with a safety switch to prevent the user from being exposed to high-voltage DC. Firstly, the PVDF-HFP mixture was processed by adding the 10% (w/v) PVDF-HFP powder to a DMF/acetone mixture (3:7) and stirring continuously for 2 h at 80 °C with a magnetic stirrer. The resulting solution was then obtained by inserting the calcined PMN-35PT ceramic powder at a concentration of 30% by volume into the PVDF-HFP mixture and then the mixture was magnetically stirred at 50 °C for a further 2 h to get a homogeneous solution. Afterward, the PVDF-HFP/%30vol.PMN-35PT solution was put into the plastic syringe, with the distance between the collector and the needle measuring approximately 15 cm. During the electrospinning process, a Taylor

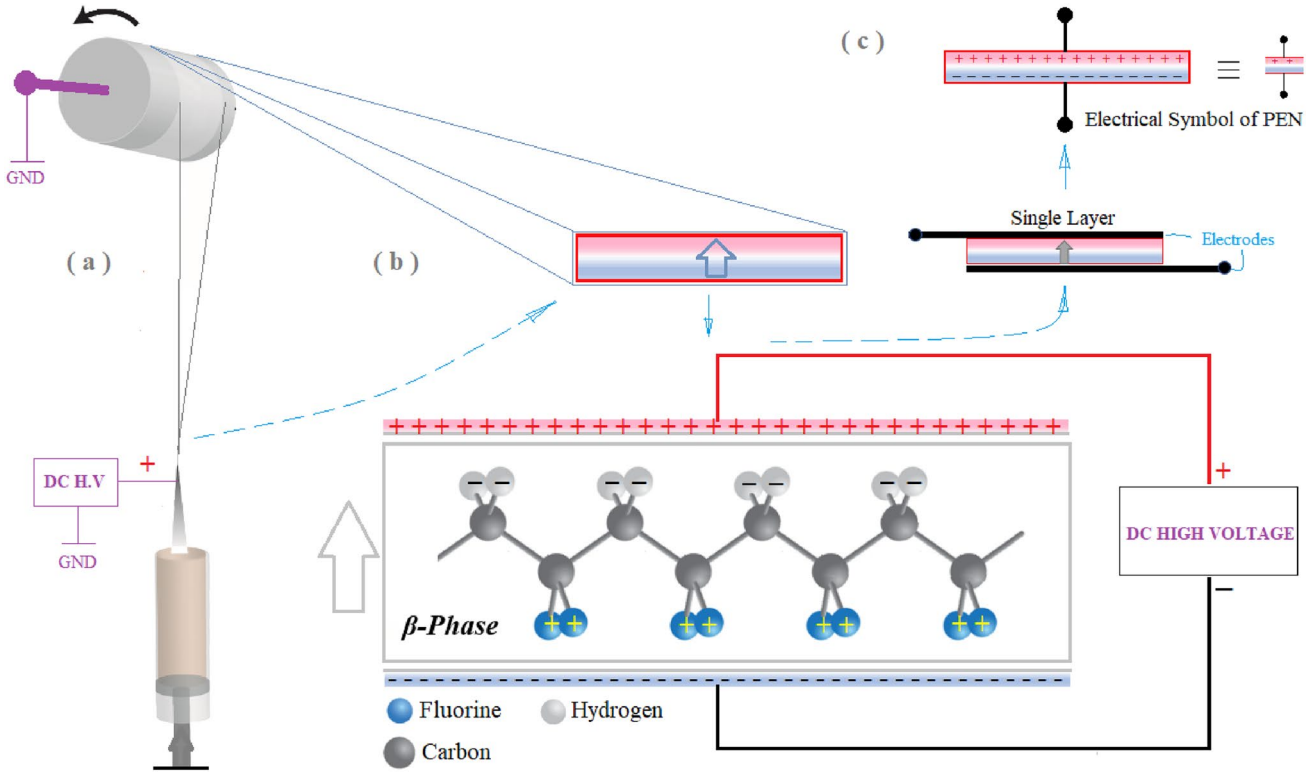

Fig. 1 The schematic presentation of the PVDF-HFP/PMN-PT fiber mat obtained through electrospinning (**a**), abstract diagram of a polymer based on β-PVDF-HFP induced by stretching and DC high poling voltage (**b**), and electrical symbol of PNG with a single layered (**c**)

cone is created by directing the meniscus of the solution at the end of the needle when a high DC voltage of 15 kV is applied between the needle tip and the collector wrapped in aluminum foil. When the high electric field reaches a certain critical value, the electrostatic force acts in the opposite direction, overcoming the surface tension and ejecting the polymer solution from the Taylor cone toward the rotating drum collector toward the rotating drum collector. Throughout this transmission, the polymer solution adheres as charged fiber mat form by drying to the surface of the rotating drum collector. Furthermore, for the time of the process, the fluorine and hydrogen atoms in the chain structure of the PVDF-HFP were separated from each other by the effects of the high voltage and the stretching of the rotating drum collector. The electrospinning process contributes not only to the formation of the PVDF-HFP fiber mat with a beta phase but also to the formation of a dipole moment perpendicular to the polymer chain structure (Fig. 1b). As the resulting orientation exhibits a transition structure between α and β phases, a net polarization occurs which is responsible for the piezoelectric effect in the PVDF-HFP [36]. Hence, it is expected that the highest electrical output voltage will be obtained from the PNG device with the highest dipole moment. Afterward, the single-layered PNG (dimensions of 4 cm × 4 cm) device was fabricated by packing the PVDF-HFP/PMN-35PT electrospun mat that was placed between two conductive electrodes. Moreover, the electrical symbol of the PNG device was defined by considering the direction of the dipole moment that was formed on the electrospun mat (Fig. 1c).

2.3 Characterization

The crystalline structure and the phase of the pure PVDF-HFP and the PVDF-HFP/ PMN-35PT fiber mats were analyzed by an X-ray diffractometer (XRD, PANalytical Empyrean) with CuK radiation (1.5418 Å) at room temperature, while their surface morphology and cross-sectional images were measured using scanning electron microscopy (SEM, SUPRA 40VP). The Fourier transform infrared spectroscopy (FTIR)

spectra associated with all of the samples were examined using the Bruker FTIR-ATR system. The resulting values were in the range of 400–1600 range cm^{-1} at room temperature. The PNG devices' capacitance and impedance properties were measured through an LCR meter (HIOKI-IM3536). In order to define the piezoelectric characterization of the PNGs, the piezoelectric energy harvesting system was used. The output voltages obtained from the PNG devices versus the periodic force were defined as V_{PP} (peak-to-peak) amplitude using a data logger (NI-6009), whereas their short-circuit currents were measured via a low-noise current amplifier (LMC-6001).

3 Results and discussion

3.1 Structural characterization

The crystal structure and the phase identification of both the pristine PVDF-HFP polymer and the PVDF-HFP/PMN-35PT composite with a filler ratio of 30 vol.% are indicated in Fig. 2.

The diffraction peak at 2θ of 20.18° is associated with the β-phase in the PVDF-HFP [37], whereas the diffraction peaks of the PMN-35PT particles at 22.05° (100), 31.38° (110), 38.78° (111), 45.19° (200), 50.99° (210), 56.07° (211), and 65.54° (220) are affiliated with the perovskite structure.

The mean crystallite size of the PMN-35PT nanoparticles was calculated to be about 36 nm for the most intense peak of the (110) plane [38] using Scherrer's Eq. (1).

$$D = \frac{0.9\lambda}{\beta \cos\theta^{\circ}}, \tag{1}$$

where D is the mean crystalline size (nm), λ is the wavelength of Cu K (0.154 nm), β is the full width at half maximum intensity (FWHM) in radian and θ° is the Bragg angle (°) [38].

The degrees of crystallinity of the samples were also determined from the XRD patterns. The degree of crystallinity (χ_c) can be calculated through Eq. (2) [39].

$$\chi_c(\%) = \frac{A_c}{A_c + A_c} \times 100, \tag{2}$$

where Ac is the area under the peaks representing the total crystalline region, while Aa is the area under the peaks representing the total amorphous region.

As the PMN-35PT has a fully crystallized perovskite structure, the XRD results demonstrate the presence of the β-phase both the PVDF-HFP and all the typical PMN-35PT peaks (χ_C: 53.55). As the size of the PMN-35PT peaks increases, the β-phase of the PVDF-HFP diffraction peak at 20.18° seems to decrease. In reality, the presence of the β-phase PVDF-HFP is preserved (χ_C: 40.14). This situation is also supported by the FTIR graph which shows an enrichment of the β-phase PVDF-HFP and PVDF-HFP/PMN-35PT [40].

FTIR spectra analyses are shown in Fig. 3 which were performed to investigate further the structure and crystalline properties of the pure PVDF-HFP and the composite based on the PVDF-HFP/PMN-35PT.

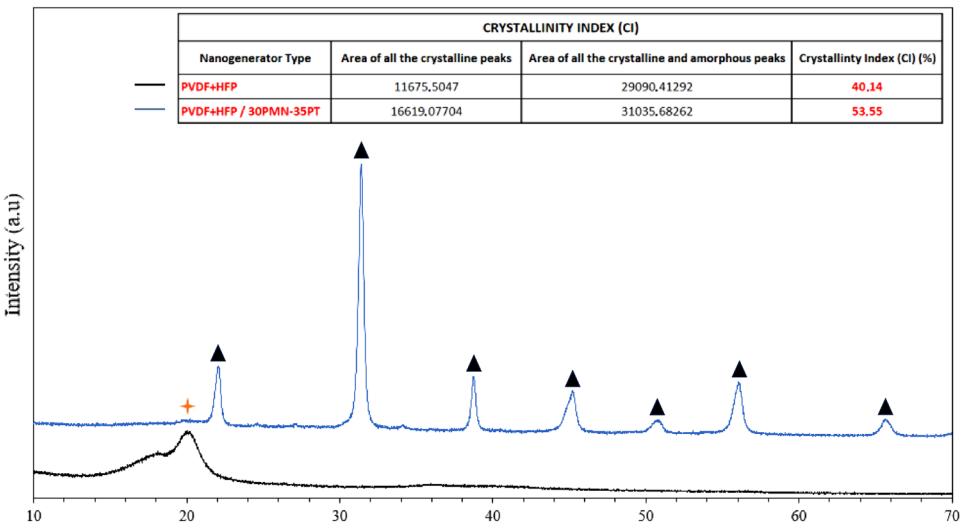

Fig. 2 XRD patterns of the neat PVDF-HFP and the PVDF-HFP/PMN-*35*PT electrospun with the PMN-35PT loading concentration of 30vol.% (✦: β-phase, ▲: Perovskite structure)

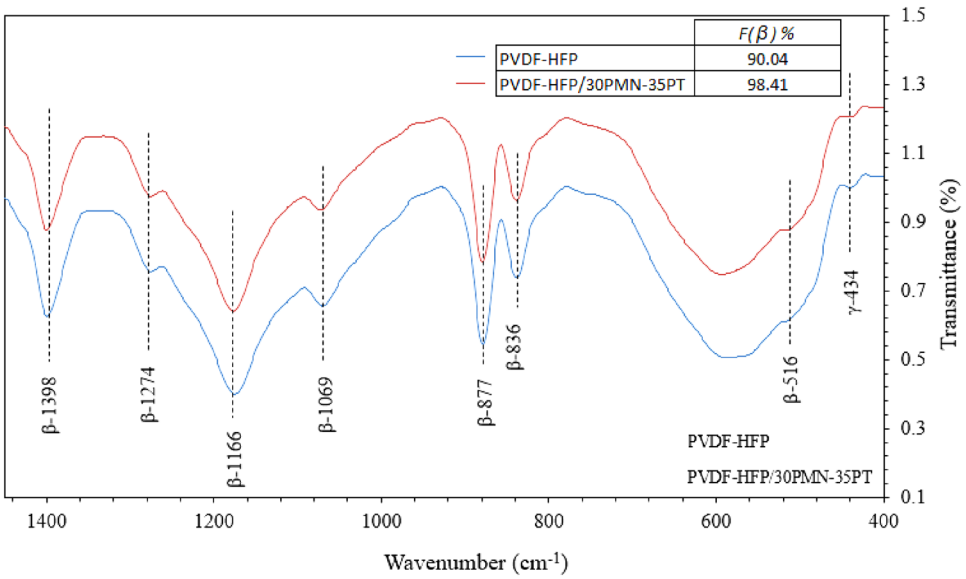

Fig. 3 FTIR spectra of the pure PVDF-HFP and the PVDF-HFP/30vol.%PMN-35PT composite

The β-phase fraction of the composites can be calculated according to the two different vibration bands (762 cm^{-1} for the α-phase and 840 cm^{-1} for the β-phase) via the following Eq. (3):

$$\%F(\beta) = \frac{A_\beta}{1.26A_\alpha + A_\beta} \times 100. \quad (3)$$

The A_α and A_β absorption coefficients are expressed by K_α (6.1×10^4 cm^2/mol) and K_β (7.7×10^4 cm^2/mol), respectively, at the particular wavenumber [41].

It is also determined via Eq. 3 that the PVDF-HFP/30PMN-35PT electrospun composites had the maximum $F(\beta)$% with a value of 98.41% compared to the pristine PVDF-HFP's $F(\beta)$% value of 90.04% (Fig. 3).

The peaks observed in Fig. 3 at bands 516 [42], 836 [43], 877 [44], 1069 [45], 1166 [46], 1274 [47], and 1398 [48] cm^{-1} of the host PVDF-HFP and the PVDF-HFP/30PMN-35PT electrospun fibers are associated with the crystalline β-phase, whereas the peak at band 434 [49] of the samples is assigned to the crystalline γ-phase. Therefore, we can say that the mechanical stretching of the fibers by the rotating drum collector supports the formation of the crystal array on the fibers during the electrospinning process [50].

3.2 Morphology analysis

The SEM graphs associated with the pure PVDF-HFP electrospun fiber and the PVDF-HFP/PMN-35PT composite with a filler ratio of 30 vol% are indicated in Fig. 4.

Figure 4b shows the homogeneous distribution of the PMN-35PT perovskite powders in a regularly oriented polymer matrix. When the PMN-35PT powder concentration was increased by 30% by volume, it was observed that the average fiber diameters of the PVDF-HFP/PMN-35PT fibers were reduced by 309 nm compared to the pure PVDF-HFP fiber diameters of around 324 nm (Fig. 4a). The decrease in the average fiber diameter of the composite based on the PVDF-HFP/PMN-35PT compared to the PVDF-HFP is compatible with the increase in crystallinity caused by the PMN-35PT ceramic powder observed in the XRD analysis.

3.3 Layer-by-layer assembly of multilayered PNGs

In order to improve the electromechanical performances of ceramic-based structures, multilayer fabrication studies have recently been emphasized [51–53]. Considering the fact that the output signal may be weak and unstable owing to the loose nature of the electrospun mat based on the PVDF-HFP/PMN-35PT with a single layered, it was decided to fabricate multilayered PNGs using a pressing process that compresses the electrospun fibers together. Figure 5, which includes the PNG's overall components, shows the fabrication stages of the multilayer PNG.

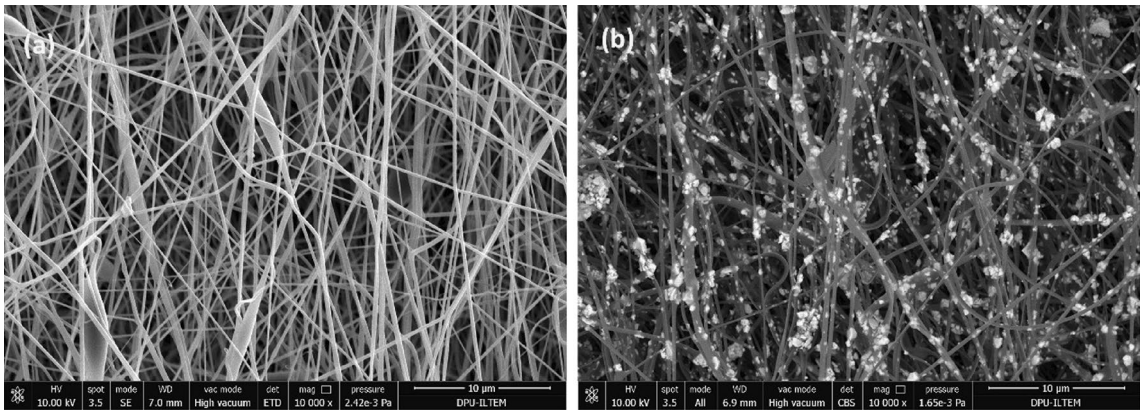

Fig. 4 SEM graphs of the pure PVDF-HFP (**a**) and the PVDF-HFP/30vol.%PMN-35PT (**b**)

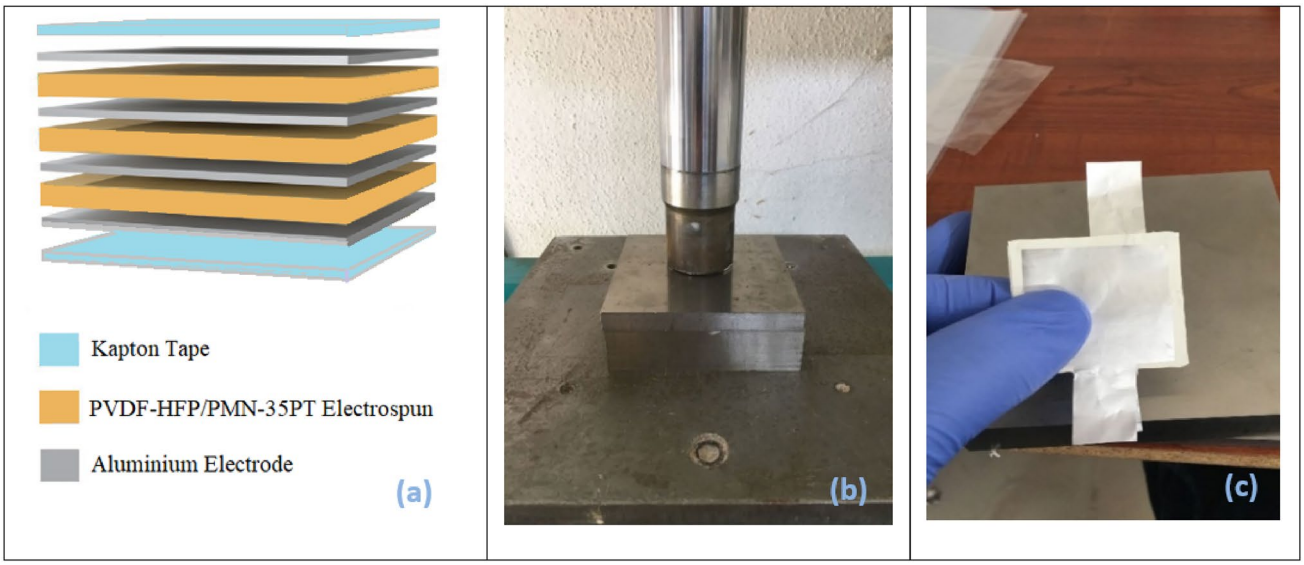

Fig. 5 The fabrication stages of the multilayered PNG. The schematic structure of the PNG (**a**). Pressing process (**b**). Photograph of the pressed fiber mats (**c**)

In order to support the flow of electrons, aluminum sheets were employed on both the top and the bottom electrodes and also on electrodes between the fiber composite layers (Fig. 5a). The fiber mats were prepared (dimensions: 4 cm × 4 cm) in various configurations of 2, 4, and 6 layers, each of which was compressed by the pressing process at room temperature under 15 MPa for 60 min (Fig. 5b, c). Then, the conductive wires were attached to the surfaces of the top and the bottom electrodes using a glue silver. Afterward, all samples were fully covered with thin Kapton tape to preserve the flexibility and stability of the multilayered PNG in a sandwich structure. Finally, as a means to realize further smooth and uniform packaging structure, the structure protected by Kapton tape was laminated with the PVC (Poly (vinyl chloride) film thickness of 125 microns using a commercial laminator (Mapilam-LM153 Model Laminating Machine with Cylinder) at a temperature of 120 °C.

As seen in Figs. 6, 7, and 8, the multilayer fabrications which include series, parallel, and combined series-parallel structures were tested to evaluate the open-circuit voltage and the short-circuit current alterations of the PNG by considering the directions of their dipole moments.

SEM images associated with the single-layered and the multilayered electrospun fibers are indicated in Fig. 9. The mean layer thickness of the single-layered

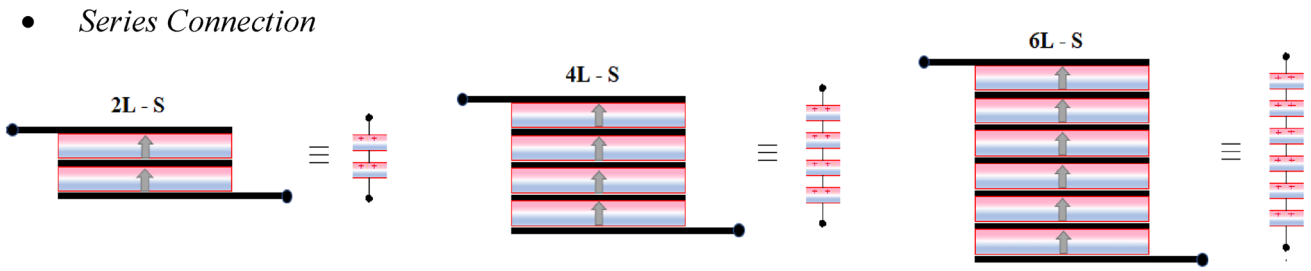

Fig. 6 Configuration of multilayered PNGs (two, four, and six layered) with a series connection and their electrical circuit equivalents

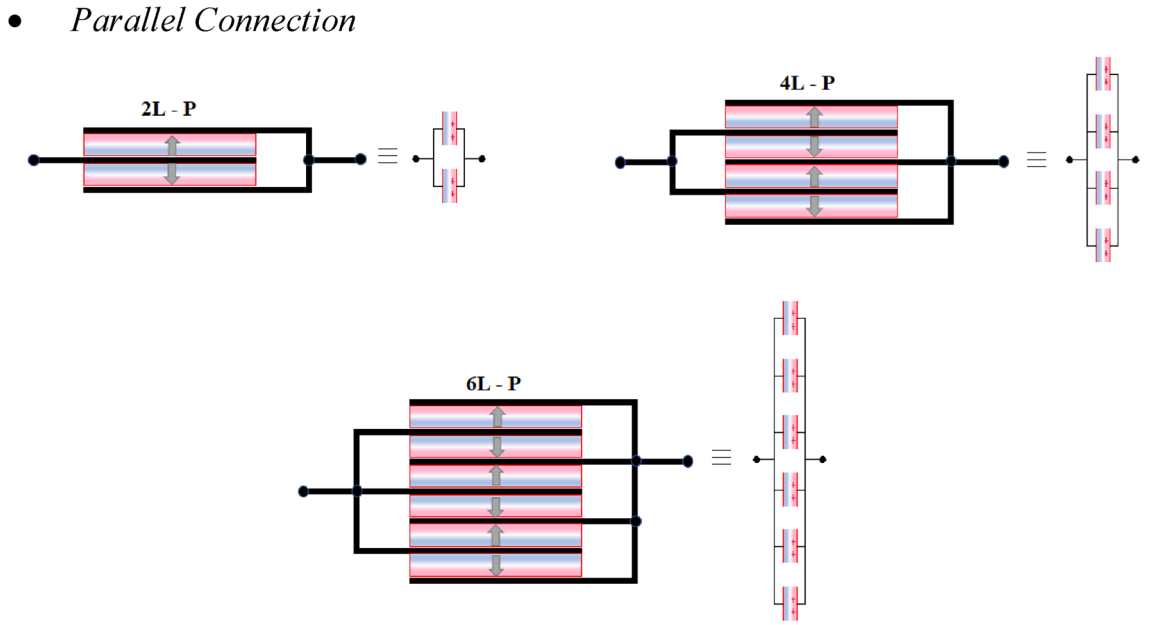

Fig. 7 Configuration of multilayered PNGs (two, four, and six layered) with a parallel connection and their electrical circuit equivalents

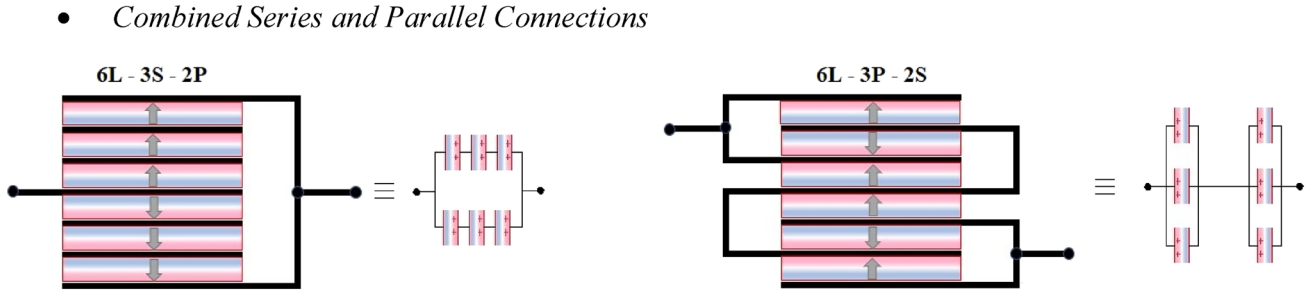

Fig. 8 Configurations of multilayered PNGs (the six layered) with a combined series-parallel connection and their electrical circuit equivalents

uncompressed PVDF-HFP/PMN-35PT was defined as about 164 μm from the cross-sectional view (Fig. 9a) and its compressed approximate thickness was measured as average 57 μm (Fig. 9b). The surface image of the four-layered PVDF/PMN-35PT composite reveals that the fibers on the surface layer have been squeezed together and the fiber density on the surface has been increased (Fig. 9c). Furthermore, within the volume of the PVDF-HFP nanofibers, the accumulation of the PMN-35PT ceramic particles (indicated as white dots

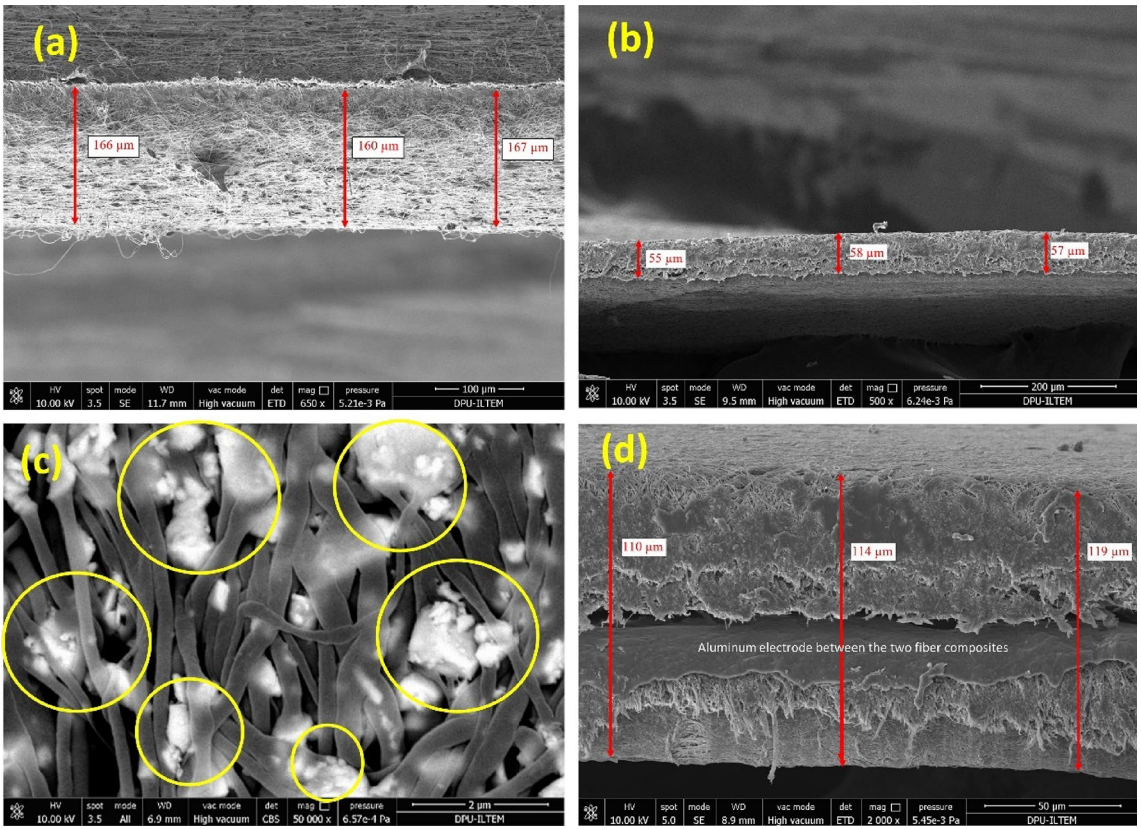

Fig. 9 SEM graphs of the surface fibers and cross-section with single-layered and multilayered electrospun fibers. **a** A cross-section of the uncompressed single-layered PVDF-HFP/PMN-35PT, **b** a cross-section of the compressed single-layered PVDF-HFP/PMN-35PT, **c** compressed surface SEM of the four-layered PVDF-HFP/PMN-35PT, and **d** a cross-section of the compressed two-layered PVDF-HFP/PMN-35PT

within yellow circles) was also observed (see Fig. 9c). As shown in Fig. 9d, the structure with the aluminum electrode placed between the two fiber composite layers was well pressed and its total thickness was approximately 114 µm.

3.4 Output performances of multilayered PNGs

In order to evaluate the output performance of the PNG, a two-port network system which can be simplified using advanced techniques such as the Thevenin's, the Norton's, and the maximum power transfer theorems was utilized. Figure 10 shows the Thevenin, Norton, and the maximum power transfer equivalent circuits associated with the PNG.

A PNG device is defined as the Thevenin equivalent voltage V_{TH} (open-circuit voltage V_{OC}) and the Thevenin equivalent resistance R_{TH} connected in a series with a V_{TH} voltage source (Fig. 10a). According to Thevenin theorem, Thevenin's voltage V_{TH} is also the open-circuit voltage V_{OC} of the PNG measured at the network output ($V_{TH} = V_{OC}$ and $R_{TH} = \infty$). If the independent energy sources were turned off, Thevenin's resistance R_{TH} would equal the resistance that is measured between the PNG's output terminals [54]. Furthermore, the same PNG device can also be shown by the Norton equivalent current I_{NT} and the Norton equivalent resistance R_{NT} connected in parallel with an I_{NT} current source (Fig. 10b). Considering the Norton theorem, Norton's current I_{NT} is also a short-circuit current I_{SC} when the PNG leads are shorted (red line) at the network output ($I_{NT} = I_{SC}$, and $R_{NT} = 0$). If the independent energy source-I_{NT} were turned off, Norton's resistance R_{NT} would equal the resistance that is measured between the PNG's output terminals [54]. Therefore, we can say that Norton's resistance is the same as Thevenin's resistance ($R_{TH} = R_{NT}$). Considering the relationship

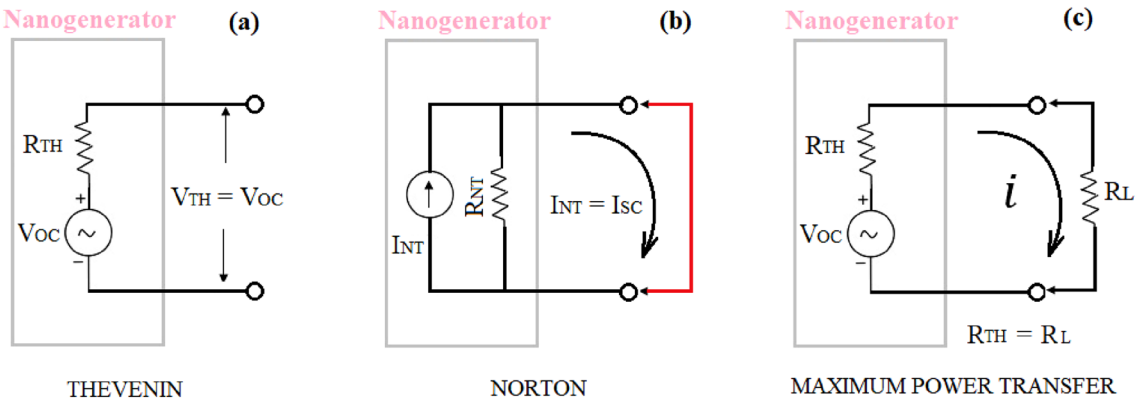

Fig. 10 Thevenin (**a**), Norton (**b**), and maximum power transfer (**c**) equivalent circuits of a PNG

between the Thevenin and the Norton theorems, we can deduce the following Eq. (4).

$$R_{TH} = \frac{V_{OC}}{I_{SC}}. \tag{4}$$

In order to get electrical power from a PNG, a load resistance R_L is connected in parallel to the nanogenerator leads as shown in Fig. 10c.

According to Fig. 10c, the electrical power on the load R_L can be expressed by the following Eq. (5).

$$P = i^2.R_L = \left(\frac{V_{TH}}{R_{TH} + R_L}\right)^2.R_L. \tag{5}$$

As specified by the "Maximum Power Transfer" theorem, since the maximum power is transferred to the load when the load resistance R_L is equal to the Thevenin resistance R_{TH}, and Thevenin's voltage V_{TH} is also the open-circuit voltage V_{OC} of the PNG, the maximum power can thus be calculated using the following Eq. (6).

$$P_{max} = \left(\frac{V_{OC}^2}{4R_{TH}}\right). \tag{6}$$

Figure 11 shows the experimental setup of the piezoelectric harvesting system which used to determine the piezoelectric performance of the PVDF-HFP/PMN-35PT-based PNG, which varies proportionally with the mechanical sensing performance and shows all the photographs of the fabricated PNGs.

The piezoelectric energy harvesting system consists of an aluminum cantilever beam and a magnetic shaker which vibrates this aluminum cantilever beam at a suitable amplitude via a power amplifier and at the desired frequency by a frequency generator. Experimental data were displayed through the graphical user interface based on the NI LabView™ Software.

In the experimental setup, the first step was to measure the open-circuit voltages of the PNGs by computer-aided measurement using the NI-6009 data acquisition unit which has an input impedance of > 1MΩ (S1 = ON, S2 = OFF, S3 = OFF, and S4 = OFF). In the next step, the PNGs with the best performance in terms of open-circuit measurement results were selected and then their short-circuit current performances were defined using a low-noise current amplifier based on the LMC-6001 (S1 = OFF, S2 = ON, S3 = ON, and S4 = OFF).

The open-circuit voltages were calculated by $V_{RMS} = \sqrt{\frac{1}{T}.\int_0^T Voc(t)^2 dt}$, where V_{RMS} = the effective voltage, V_{OC} = the voltage measured when the electrode leads are open circuited, and T = the periodic time. The short-circuit currents were defined as $I_{RMS} = \sqrt{\frac{1}{T}.\int_0^T Isc(t)^2 dt}$, where I_{RMS} = the effective short-circuit current, I_{SC} = the current measured when the electrode tips are shorted, and T = the periodic time.

The output voltage changes (depending on the time) for all PNGs are indicated in Figs. 12, 13, and 14, respectively. Furthermore, Figs. 12, 13, and 14 show 500 data per second for each vibration frequency value such as 5, 10, 15, 20, and 25 Hz and a total of 2500 data per second for each nanogenerator. It can be seen in detail in Fig. 13 that the voltages obtained from the nanogenerator are changed in real time when the voltage changes in the narrow region are shown by expanding as 11,000 data on a single graph.

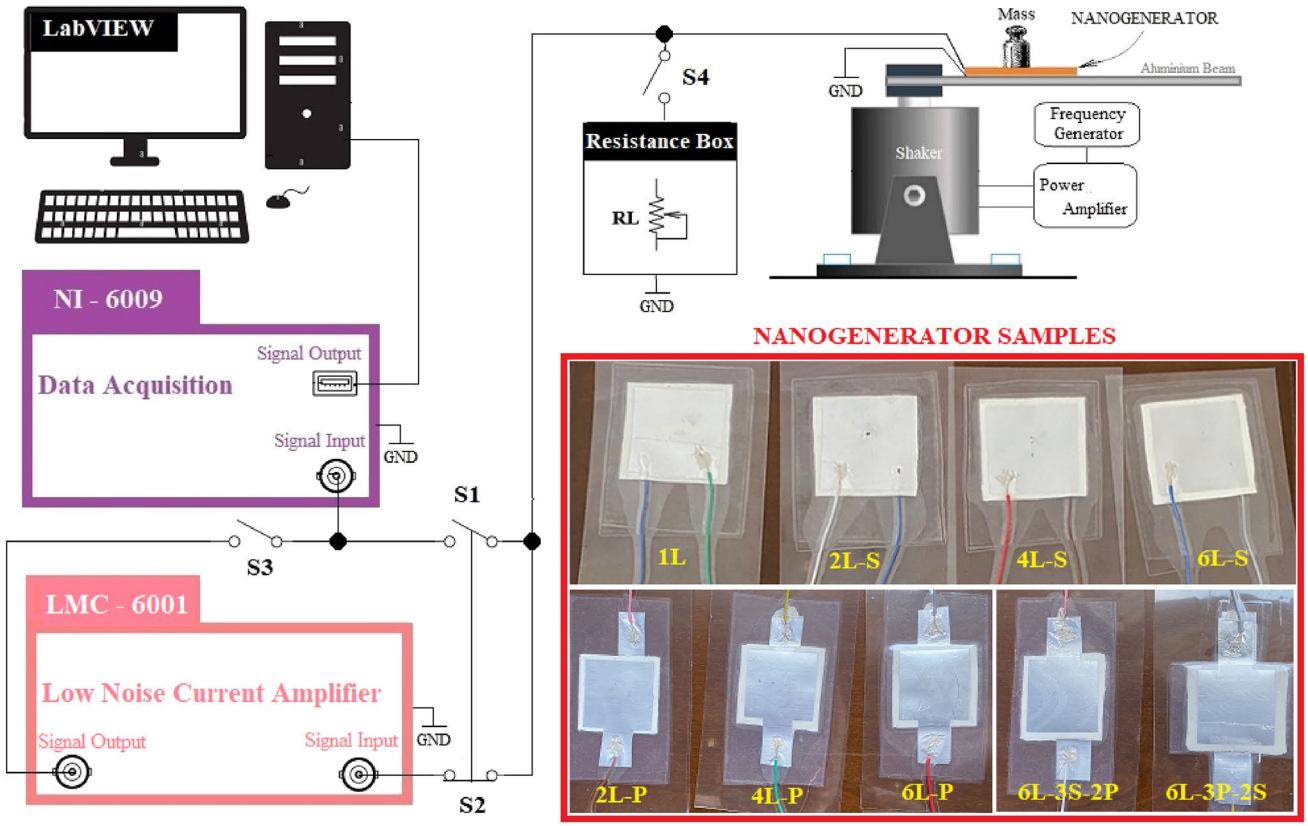

Fig. 11 Experimental setup for the piezoelectric energy harvesting system and photographs of the fabricated PNG samples

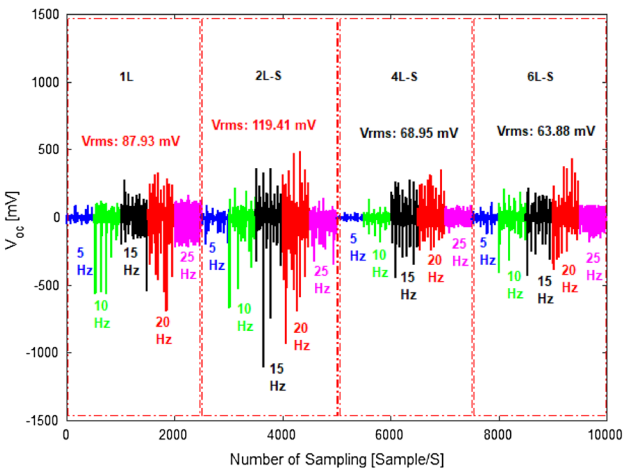

Fig. 12 The V_{RMS} and the V_{OC} alternations of the single- and multilayered PNGs with a series connection (1L, 2L-S, 4L-S, and 6L-S)

The highest V_{RMS} values of 119.41 mV at 20 Hz for the two-layered PNG with a series connection and 408.07 mV at 20 Hz for the four-layered PNG with a parallel connection were measured as compared to the single-layered PVDF-HFP sample (1L). Furthermore, considering that the multilayered combined series-parallel connections, measured as the V_{RMS} value of 69.59 mV at 15 Hz for 6L-3P-2S, was higher than that of the 6L-3S-2P, it was chosen.

As seen in Fig. 15, considering that the I_{RMS} changes associated with the single- and multilayered PNGs (1L, 2L-S, 4L-P, and 6L-3P-2S) were measured, while their electrode tips were shorted, the maximum I_{RMS} value of 2.91 μA was reached for the four-layered PNG with a parallel connection.

The I_{RMS} and the P_{MAX} changes of the single- and multilayered PNGs are given in Fig. 16.

Assessing all of the measurement results, maximum electrical power of 0.3 μW was achieved by drawing a 1.46 μA current under a resistive load of 140.2 KΩ from the four-layered PNG with a parallel connection.

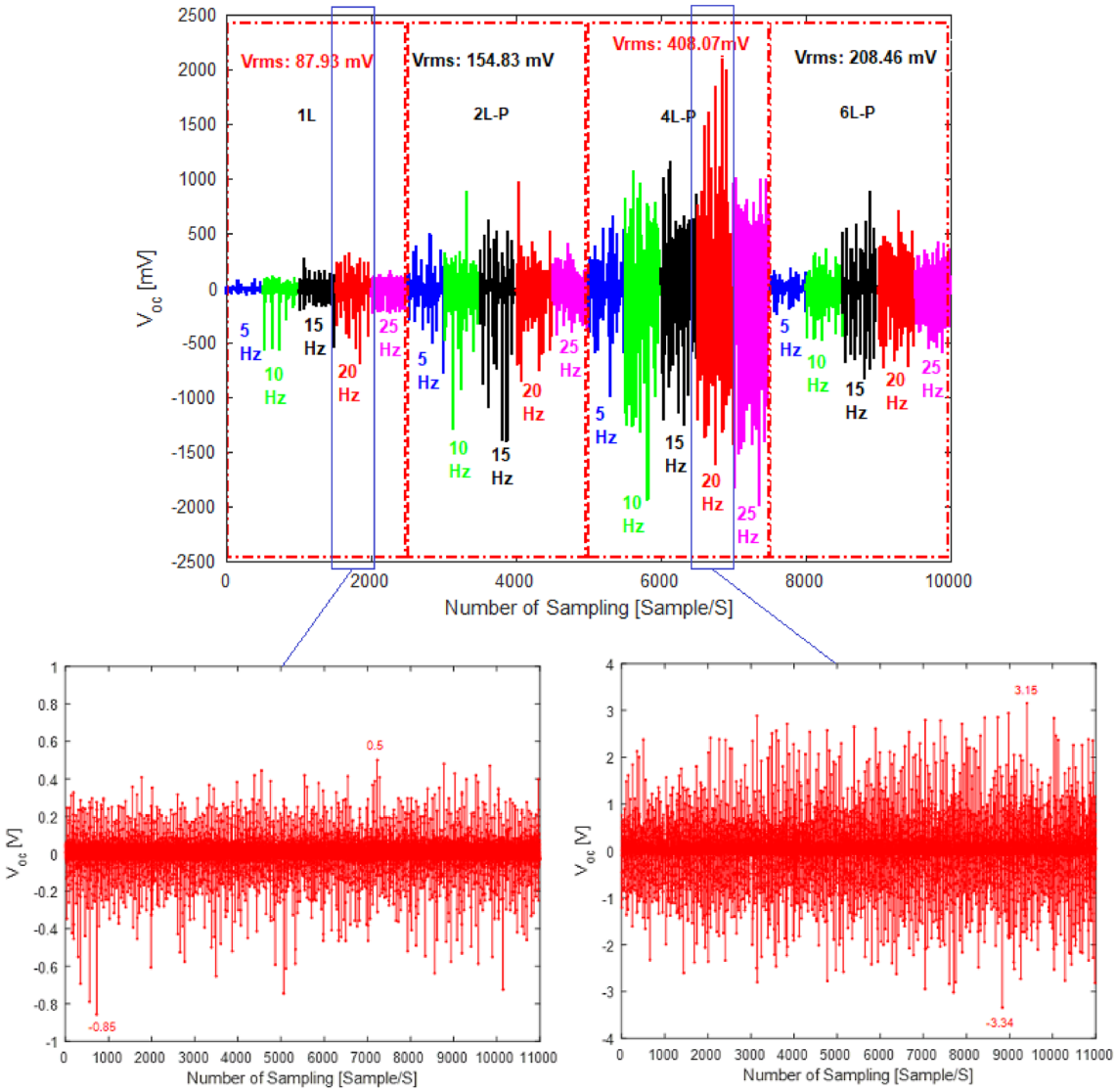

Fig. 13 The V_{RMS} and the V_{OC} alternations of the single- and multilayered PNGs with a parallel connection (1L, 2L-P, 4L-P, and 6L-P)

3.5 Capacitance and impedance properties of multilayer PNGs

The output voltage dependent on the piezoelectric charge coefficient- d_{33} of the PNGs can also be expressed by Eq. (7).

$$Q = N.d_{33}.F, \tag{7}$$

where d_{33}, N, F, and Q show the piezoelectric charge coefficient of a single-layer PEN, the number of layers, the force (F) applied to the multilayer PNG, and the accumulated charge on the PNG, respectively.

The capacitance of the multilayer PNG can be described by the following Eq. (8) [55].

$$C = \left(N.A.\varepsilon_{33}.\varepsilon_0\right)/t, \tag{8}$$

where N, A, ε_{33}, ε_0, and t depict the number of layers, the electrode area, the dielectric constant, the free space's dielectric constant (8.85×10^{-12} F/m), and the thickness of a single layered, respectively.

Finally, the open-circuit voltage (V_{OC}) of the multilayer PNG generated from its applied force can be written by Eq. (9).

$$V_{oc} = \frac{Q}{C} = \frac{d_{33}.t}{A.\varepsilon_{33}.\varepsilon_0}.F^2. \tag{9}$$

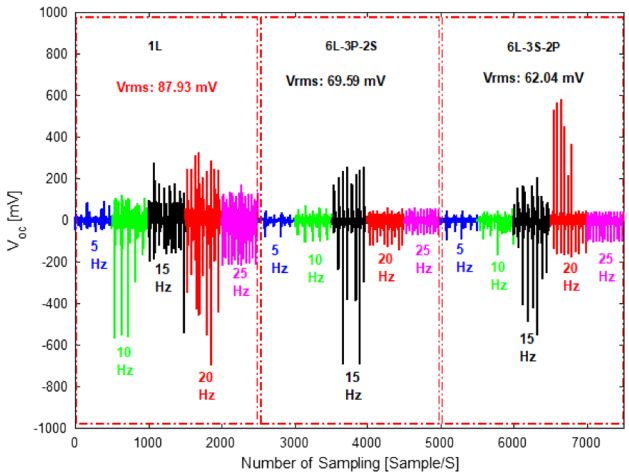

Fig. 14 The V_{RMS} and the V_{OC} alternations of the single- and multilayered PNGs with a combined series-parallel connection (1L, 6L-3P-2S, and 6L-3S-2P)

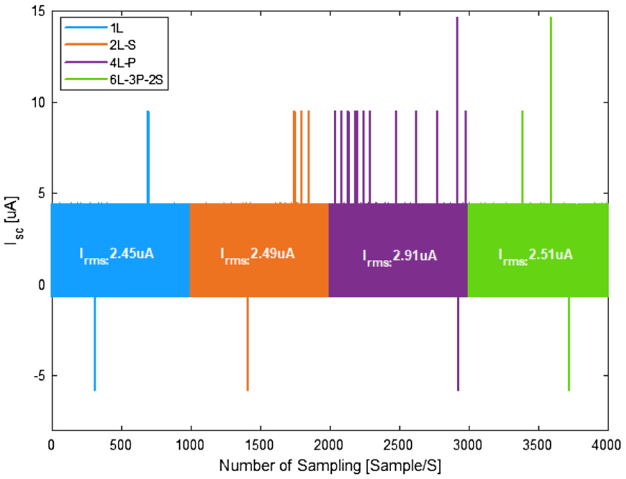

Fig. 15 The I_{RMS} and I_{SC} changes of the single- and multilayered PNGs (1L, 2L-S, 4L-P, and 6L-3P-2S)

According to Eqs. 8 and 9, the energy stored (E) in the multilayer PNG (or capacitor) can be expressed by the following Eq. 10.

$$E = \frac{1}{2}.C.{V_{oc}}^2 = \frac{N.d^2{}_{33}.t}{2\mathrm{A}.\varepsilon_{33}.\varepsilon_0}.F^2. \quad (10)$$

According to Eqs. 7 and 8, the capacitance of the multilayer PNG and Q-charge induced on it will be enhanced depending on the value of N.

Therefore, based on Eq. (9), notwithstanding the fact that the output voltage will remain unchanged depending on the number of layers, the measured voltage value slightly increases with the N. In this study, placing aluminum electrode sheets between the fiber composite layers can cause an increase in the polarization charges on the layer surfaces in three-dimensional structures [56].

The capacitance-C and the impedance-Z changes of single-layer and multilayer PNGs are shown in Fig. 17.

According to $Z = \frac{1}{2\pi \mathrm{f} C}$ (f: the measurement frequency), the four-layer PNG with a parallel connection increased its capacitance value by decreasing its impedance value, while the two-layer PNG with a series connection decreased its capacitance value by increasing its impedance value, when compared with the single-layer PNG (1L) [57]. The highest capacitance value of 550 pF was reached for the four-layer PNG with a parallel connection (2.2 times compared with the single-layered PNG). Various combinations of series and parallel connections can be used to achieve

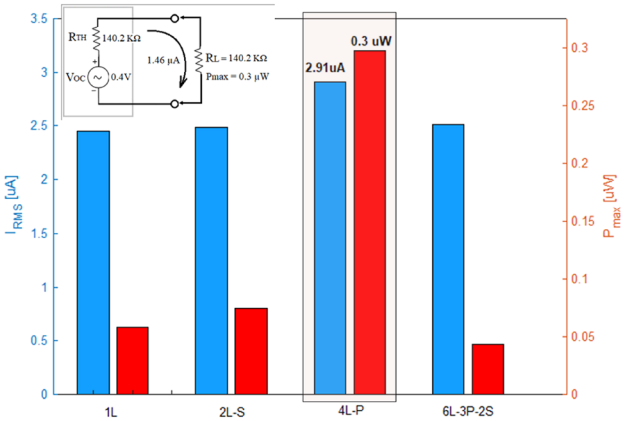

Fig. 16 The I_{RMS} and the P_{MAX} changes of the single- and multilayered PNGs (1L, 2L-S, 4L-P, and 6L-3P-2S)

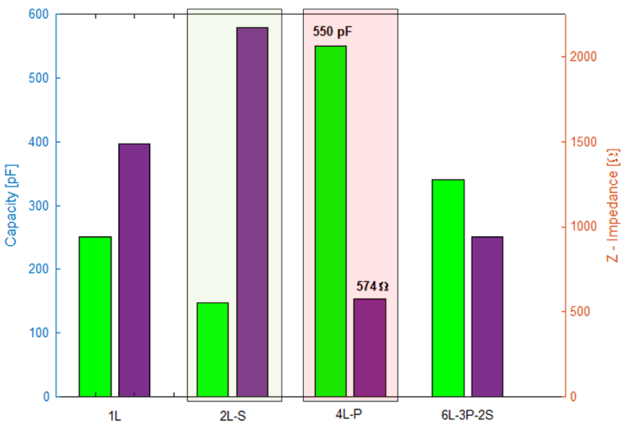

Fig. 17 The capacitance and the impedance changes of the single- and multilayered PNGs (1L, 2L-S, 4L-P, and 6L-3P-2S)

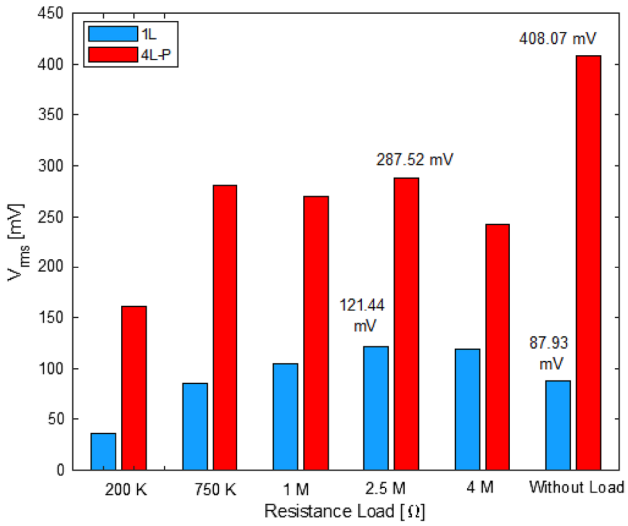

Fig. 18 The V_{RMS} changes of the single-layered PNG and the four-layered PNG with a parallel connection at a vibrational frequency of 20 Hz without a resistive load, under various resistive loads

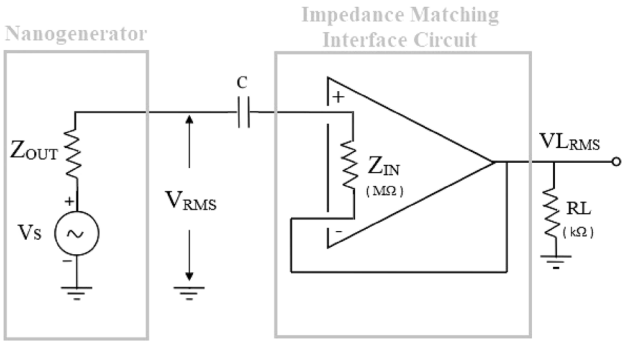

Fig. 19 The connection of the PNG to an impedance matching interface circuit

the desired capacitance and impedance values in the composite structure.

3.6 The output signal enhancement of the PNG

The PNG's output impedance accommodates a complex form that includes active-reactive components, such as a resistor, a capacitor, and an inductor. In order to obtain the maximum electrical voltage from a PNG device (i.e., minimize the output signal noise), firstly it is necessary to define its output impedance. Therefore, the V_{RMS} values on the PNGs were measured under the resistive loads from 200 KΩ to 4.5 MΩ using the piezoelectric energy harvesting system as shown in Fig. 11, sequentially (S1 = ON, S2 = OFF, S3 = OFF and S4 = ON).

Figure 18 depicts the output voltage changes of the single PNG and the four-layered PNG with a parallel connection. These voltage changes were measured under load resistances from 200 KΩ to 4 MΩ at a vibrational frequency of 20 Hz.

According to Fig. 18, the output voltages for the single-layer and the four-layered PNGs decreased with a decreasing load resistance. For the PNG's, the impedance matched the load resistance, as the highest output voltage was obtained. The maximum output voltage values under the 2.5-MΩ resistive load were measured at 287.52 mV for the four-layered PNG (parallel connection) and at 121.44 mV for the single-layered PNG.

In order to power portable electronic devices, piezoelectric energy harvesting systems, which harvest electrical energy from various vibration sources, typically focus on low-level energy harvesting in the microwatt (μW) to milliwatt (mW) range [58]. The four-layered PNG with a parallel connection which has the highest electrical power of 300 nW (Fig. 16) and a maximum output voltage of 287.52 mV under the impedance of 2.5 MΩ (Fig. 18) is not a suitable candidate to be used directly as an energy harvesting system at the microwatt-μW level. Hence, to maximize power transfer or minimize signal reflection (for the highest signal/noise ratio), it is necessary that the electrical voltages obtained from the PNG device with a high impedance can be transferred using the impedance matching systems (the voltage follower or impedance transformer) to the load with a low impedance [59]. In this study, the voltage follower based on AD620 which has high input and low output impedance properties was chosen to provide the impedance matching between the PNG device and the load. The connection diagram of a PNG to a buffer amplifier (voltage follower) is depicted in Fig. 19.

A buffer amplifier consists of a standard operational amplifier that is activated by a short circuit between the output line and the negative (inverting) input line. When the PNG device is connected to the buffer amplifier's positive input lead, the V_{RMS} input voltage is transferred via the VL_{RMS} output voltage to the load resistance KΩ because of the feedback resistance Rf equals zero [59].

Figure 20 shows a comparison of the electrical performances, such as effective voltage (V_{RMS}) and

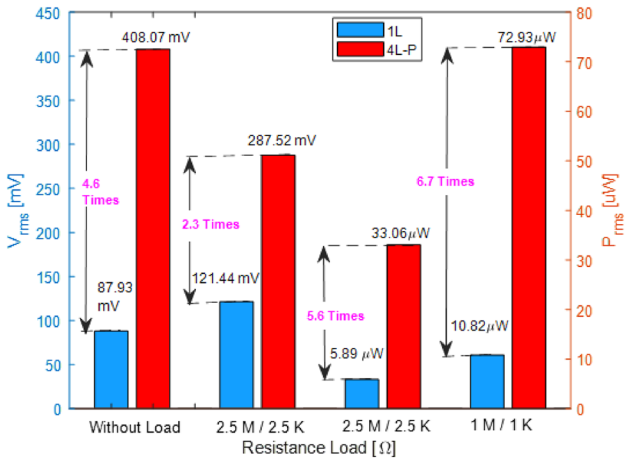

Fig. 20 Electrical performances between the single- and the four-layered PNGs at a vibrational frequency of 20 Hz without a resistive load, 1 MΩ, and under a 2.5-MΩ resistive loads

electrical power (P_{RMS}), between the single-layered and the four-layered PNGs.

According to $P_{RMS} = \frac{(VL_{RMS})^2}{RL}$, which takes into consideration the electrical behaviors of the nanogenerators both under 1-MΩ and 2.5-MΩ resistive loads, the electrical power of the four-layered (parallel connection) PNG was 6.7 times higher than that of the single-layered PNG under a resistive load of 1 MΩ/1 KΩ.

A comparison of performances between multilayered nanogenerators in the present study and different content multilayered nanogenerators in literature has been listed in Table 1 [25, 29, 60, 61].

Table 1 Comparison of performances between multilayered nanogenerator in the present study and different content multilayered nanogenerators in literature

Composite samples (year)	Fabrication method	F-β (%)	The impact force	The number of layers	The electrical power	Improvement as compared to single layer	References
PVDF/20-wt.%$BaTiO_3$ thickness: 120 μm dimensions: 2.5 cm × 2.5 cm (2021)	Spin coating	–	–	4-layered	11.55 μW (5MΩ)	6.5 times	[60]
PVDF/PZT thickness: 220 μm dimensions: 2 cm x 4 cm (2022)	Electrospinning	83.16	5N	4-layered	136.9 μW (10MΩ)	6.5 times	[25]
PVDF/aluminum (separator) thickness: 520 μm dimensions: 2 cm x 2 cm (2022)	Electrospinning	87	2.65N	2-layered	–	4.7 times	[29]
PVDF/ZnO100% thickness: 41 ± 10 μm dimensions: 2 cm x 2 cm (2023)	Electrospinning electrospray	81.4	750 kPa	5 layered (PVDF:3-L ZnO: 2-L)	– (50MΩ)	6.2 times	[61]
PVDF/30vol.%PMN-35PT aluminum (separator) Thickness ~ 220 μm dimensions: 4 cm x 4 cm (2024)	Electrospinning	98.41	1N	4-layered parallel connections	72.93 μW (1MΩ)	6.7 times	Present study

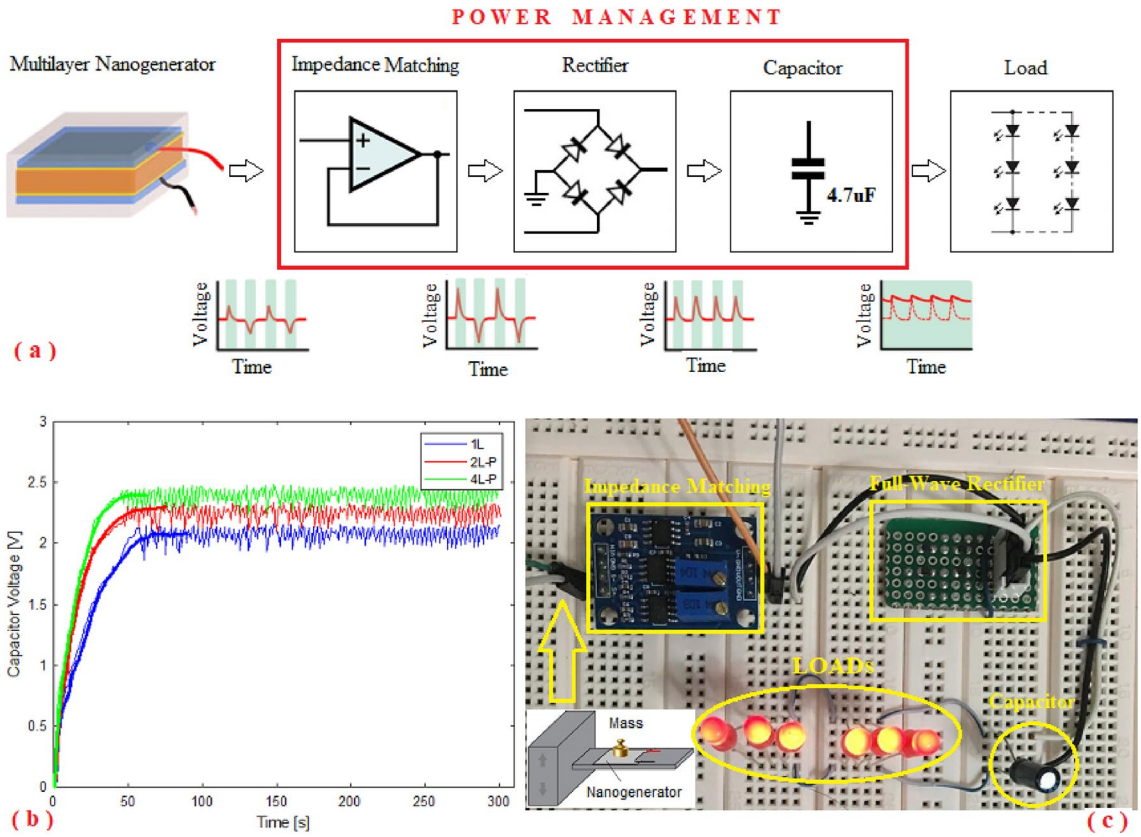

Fig. 21 Block diagram of the power management system (**a**). Time-dependent charging curves of the single-layered, two-layered, and four-layered PNGs for the capacitor value of 4.7 μF (**b**). Photograph of 6 red LEDs brightened by electrical energy generated by a four-layered PNG (**c**)

3.7 Application explorations for generation output of the PNG

3.7.1 The charging of a commercial capacitor

In order to improve the PNG, as seen illustrated in Fig. 21a, a power management system was employed. The power management system consists of the impedance matching circuit, the full-wave rectifier, the capacitor, and the loads.

In this section, a commercially available AD620 instrumentation amplifier card, which has a high input impedance (Shenzhen Zhinuo Xinda Technology Co., Ltd.), was selected as a signal conditioner for the impedance matching between the PNG and the load, also for the amplification of the small AC signals produced from the PNG. The Schottky diode (PMEG-2020AEA) was used as a full-wave rectifier (bridge type) circuit which converts AC form signals to DC form signals.

Under a vibration frequency of 10 Hz and an impact force value of 1N for 300 s, the measured voltage curves of a 4.7 μF capacitor charged by the single-, two-layered, and four-layered PNGs are indicated in Fig. 21b. Figure 21c depicts 6 commercial LEDs (light-emitting diodes) lit up by electrical energy generated by a four-layered PNG with a parallel connection. In addition, supercapacitors may be preferable for applications with rapid charge/discharge cycles, rather than lengthy energy storage.

3.7.2 An IOT application and wearable human–machine interaction (HMI) system

In recent years, the developments on IOT (Internet of Things)-based applications of wireless sensors are not only limited to buildings, machines, or vehicles but are also extended to other areas. Especially, with the development of wearable and portable devices that can be integrated into our bodies, our health

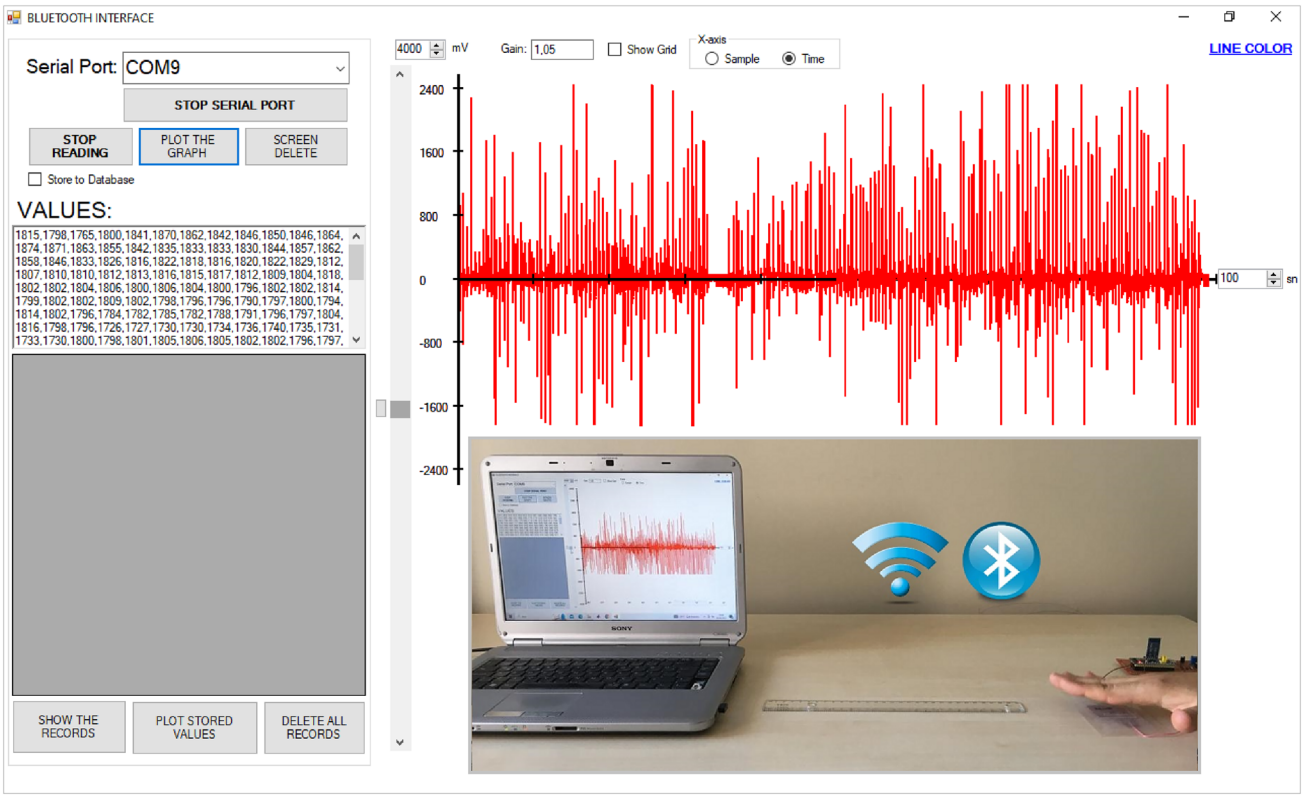

Fig. 22 A wireless monitoring system

activities, such as movement, blood pressure, breathing rate, body temperature, and heart rate, can be monitored, recorded, and analyzed in detail [62–64].

In this study, a Human–Machine Interaction (HMI) system is developed to collect data from a person using electrical signals captured from various body movements via PNG and to transmit this collected data to a computer through a wireless-based communication module. The HIM system covers some equipment, such as the instrumentation amplifier (AD620), the microcontroller (STM32F103), and the wireless module with serial communication (HC-06). The microcontroller unit was designed to convert analog signals into digital signals at sufficient rates to provide reliable synchronized data acquisition. When the wireless module is paired with a computer, all data received through the serial input of the wireless module is immediately transmitted over the air and can be monitored on the computer screen. A wireless monitoring system is depicted in Fig. 22.

The HMI system was programmed through the Keil µvision development tools at the Arduino IDE platform, while the interface program, which works compatible with Windows operating systems, was developed using the C# programming language.

The output voltage changes of the four-layered PNG with a parallel connection according to various human body movements, such as finger tapping, wrist bending, arm bending, and foot stamping, are presented in Fig. 23.

These results provide evidence that fabricated PNGs can not only be used in piezoelectric energy harvesting (mechanical vibrational energy which exists in the environment) but can also be applied the biomechanical energy harvesting (sensing various human motions).

4 Conclusions

The multilayered PVDF-HFP/PMN-35PT piezoelectric electrospun composites were successfully fabricated as a series, a parallel, and combined series-parallel configurations via the pressing process. With the evaluation of the fabricated PNGs with the Thevenin, Norton, and maximum power theorems, the four-layered PNG with a parallel connection, which has

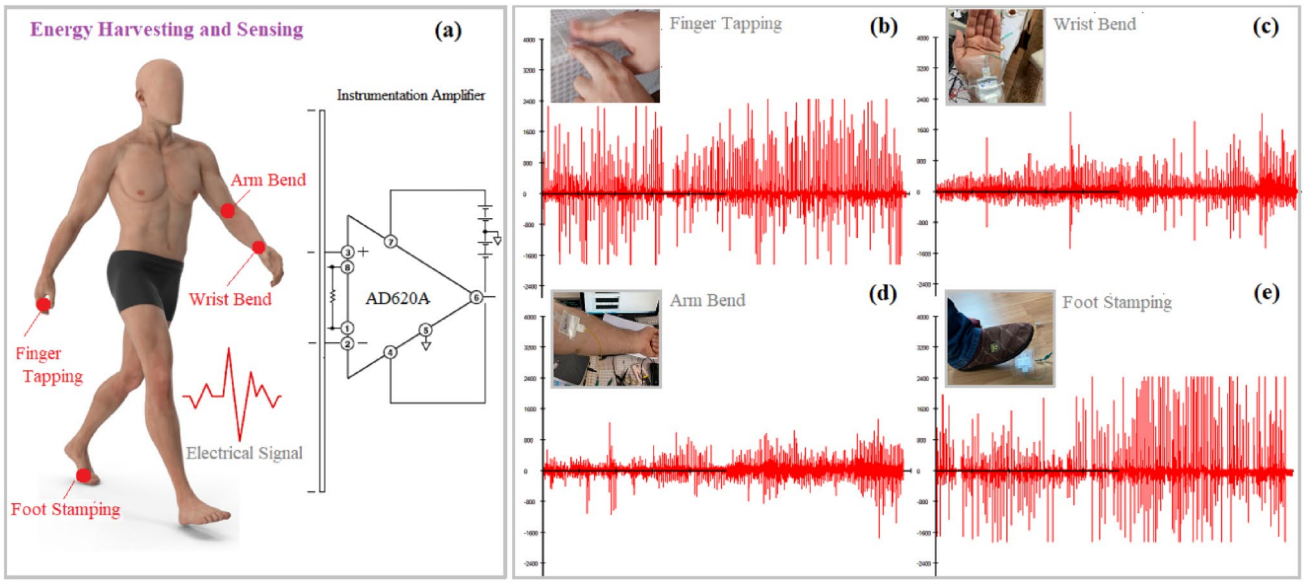

Fig. 23 The biomechanical energy harvesting performances of four-layered PNG as wearable sensor (**a**). Output voltage changes obtained during finger tapping (**b**), wrist bend (**c**), arm bend (**d**), and foot stamping (**e**)

the highest open-circuit voltage of 0.4 V (V_{RMS}) compared to the others, was found to reach a maximum power capacity of 300 nW under a resistive load of 140.2 KΩ. At the same time, the four-layered PNG connected in a parallel connection achieved a capacitance value that was 2.2 times higher than that of the single-layer PNG. Increasing on the capacitance value and decreasing on the impedance value of the four-layered PNG (connected in parallel) supports an increase in its electrical performance. In evaluations made by connecting the PNG to a voltage follower, which is used to provide impedance matching between the PNG and the resistive loads, the electrical power capacity of the four-layered (parallel connection)-based PNG possessed a better electrical power efficiency rate of 570% at a vibrational frequency of 20 Hz compared to that of the PNG with a single layered, under a resistive load of 1 MΩ. All the results emphasize that the electrical performance of the multilayer PNG device depends not only on the number of layers but also on the series, parallel, and combined series-parallel connections formed according to the dipole moment direction of their fiber mats. In addition, the PNGs which have the required voltage and current capacities can also be fabricated using various combinations of series and parallel connection types. The next study will be focused on the triboelectric effects obtained from contact gaps in multilayered piezoelectric fibers with large contacting surfaces.

Acknowledgements

This work was supported by the Scientific Research Council of Kütahya Dumlupınar University (Project No. 2023-005). The author thanks Mehmet Akkaş (Advanced Technologies R&D Center) for XRD, FTIR, and SEM analyses of PNGs and also Muhterem Koç (Kütahya Dumlupınar University) for multilayer nanogenerator fabrication and their capacitance/impedance measurements. Ertuğrul Karakulak (Tekirdağ Namık Kemal University) and Ali Sarı (Nanotech Energy Laboratory, Manisa Celal Bayar University) are gratefully acknowledged for the IOT designs and the energy harvesting measurements, respectively.

Author contributions

LP contributed to the Conceptualization, Methodology, Investigation, Data curation, Writing of the original draft, and Supervision.

Funding

Open access funding provided by the Scientific and Technological Research Council of Türkiye (TÜBİTAK). The author has not disclosed any funding.

Data availability

Data will be made available on request.

Declarations

Conflict of interest The author declares that he has no known competing financial interests or personal relationships that could have appeared to influence the work reported in this paper.

References

1. E.J. Lee, T.Y. Kim, S.W. Kim, S. Jeong, Y. Choi, S.Y. Lee, Energy Environ. Sci. **11**, 1425 (2018)
2. S. Naifar, S. Bradai, C. Viehweger, O. Kanoun, Eur. Phys. J.: Spec. Top. **224**, 2897 (2015)
3. H. Li, C. Tian, Z.D. Deng, Appl. Phys. Rev. (2014). https://doi.org/10.1063/1.4900845
4. K. Il Park, M. Lee, Y. Liu, S. Moon, G.T. Hwang, G. Zhu, J.E. Kim, S.O. Kim, D.K. Kim, Z.L. Wang, K.J. Lee, Adv. Mater. **24**, 2999 (2012)
5. X. Yan, G. Li, Z. Wang, Z. Yu, K. Wang, Y. Wu, Nano Energy (2020). https://doi.org/10.1016/j.nanoen.2020.105180
6. M. Yan, S. Liu, Q. Xu, Z. Xiao, X. Yuan, K. Zhou, D. Zhang, Q. Wang, C. Bowen, J. Zhong, Y. Zhang, Nano Energy (2023). https://doi.org/10.1016/j.nanoen.2022.108096
7. M. Li, H.J. Wondergem, M.J. Spijkman, K. Asadi, I. Katsouras, P.W.M. Blom, D.M. De Leeuw, Nat. Mater. **12**, 433 (2013)
8. J. Yang, Q. Chen, F. Xu, H. Jiang, W. Liu, X. Zhang, Z. Jiang, G. Zhu, Adv. Electron. Mater. (2020). https://doi.org/10.1002/aelm.202000578
9. G. Wang, T. Liu, X.C. Sun, P. Li, Y.S. Xu, J.G. Hua, Y.H. Yu, S.X. Li, Y.Z. Dai, X.Y. Song, C. Lv, H. Xia, Sens. Actuators A Phys. **280**, 319 (2018)
10. S.H. Shin, Y.H. Kim, J.Y. Jung, M. Hyung Lee, J. Nah, Nanotechnology (2014). https://doi.org/10.1088/0957-4484/25/48/485401
11. A. Bouhamed, Q. Binyu, B. Böhm, N. Jöhrmann, N. Behme, W.A. Goedel, B. Wunderle, O. Hellwig, O. Kanoun, Compos. Sci. Technol (2021). https://doi.org/10.1016/j.compscitech.2021.108769
12. T.H. Han, R. Nirmala, T.W. Kim, R. Navamathavan, H.Y. Kim, S.J. Park, J. Nanosci. Nanotechnol. **16**, 595 (2016)
13. R. Li, C. Xiong, D. Kuang, L. Dong, Y. Lei, J. Yao, M. Jiang, L. Li, Macromol. Rapid Commun. **29**, 1449 (2008)
14. N. Jia, Q. Xing, G. Xia, J. Sun, R. Song, W. Huang, Mater. Lett. **139**, 212 (2015)
15. S.Y. Chu, T.Y. Chen, I.T. Tsai, W. Water, Sens. Actuators A Phys. **113**, 198 (2004)
16. J. Ma, J. Hu, Z. Li, C.W. Nan, Adv. Mater. **23**, 1062 (2011)
17. M.Y. Lu, J. Song, M.P. Lu, C.Y. Lee, L.J. Chen, Z.L. Wang, ACS Nano **3**, 357 (2009)
18. S. Li, J. Zhang, D.D. Ju, X. Li, J.C. Zhang, X. Yan, H. Di Zhang, F. Song, Y.Z. Long, Chem. Eng. J. **350**, 645 (2018)
19. J. Zhang, S. Li, D.D. Ju, X. Li, J.C. Zhang, X. Yan, Y.Z. Long, F. Song, Chem. Eng. J. **349**, 554 (2018)
20. A.P. Venugopal, O. Cespedes, S.J. Russell, J. Polym. Sci. (2014). https://doi.org/10.1155/2014/102946
21. N. Chamankar, R. Khajavi, A.A. Yousefi, A. Rashidi, F. Golestanifard, Ceram. Int. **46**, 19669 (2020)
22. N. Chamankar, R. Khajavi, A.A. Yousefi, A. Rashidi, F. Golestanifard, Ceram. Int. **46**, 23567 (2020)
23. M. Kashfi, P. Fakhri, B. Amini, N. Yavari, B. Rashidi, L. Kong, R. Bagherzadeh, J. Ind. Text. **51**, 531S (2022)
24. G. Collins, J. Federici, Y. Imura, L.H. Catalani, J. Appl. Phys (2012). https://doi.org/10.1063/1.3682464
25. X. Du, Z. Zhou, Z. Zhang, L. Yao, Q. Zhang, H. Yang, J. Adv. Ceram. **11**, 331 (2022)

26. Y. Li, J. Tan, K. Liang, Y. Li, J. Sun, H. Zhang, C. Luo, P. Li, J. Xu, H. Jiang, K. Wang, J. Mater. Sci. Mater. Electron. **33**, 4291 (2022)
27. Y. Zhang, M. Xie, J. Roscow, Y. Bao, K. Zhou, D. Zhang, C.R. Bowen, J. Mater. Chem. A Mater. **5**, 6569 (2017)
28. Y.W. Kim, H.B. Lee, S.M. Yeon, J. Park, H.J. Lee, J. Yoon, S.H. Park, ACS Appl. Mater. Interfaces **10**, 5723 (2018)
29. R. Yahyapour, M.S. Sorayani Bafqi, M. Latifi, R. Bagherzadeh, J. Mater. Sci. (2022). https://doi.org/10.1007/s10854-021-07296-1
30. R. Bai, H. Shao, H. Wang, X. Ding, W. Wang, X. Jin, W. Yang, T. Lin, Mater. Today Sustain. (2023). https://doi.org/10.1016/j.mtsust.2022.100275
31. Y. Su, C. Dagdeviren, R. Li, Adv. Funct. Mater. **25**, 5320 (2015)
32. L. Paralı, M. Koç, E. Akça, Ceram. Int. **49**, 18388 (2023)
33. A.K. Singh, D. Pandey, O. Zaharko, Phys. Rev. B. Condens. Matter Mater. Phys. (2006). https://doi.org/10.1103/PhysRevB.74.024101
34. P. Augustine, M. Rath, M.S. Ramachandra Rao, Ceram. Int. (2017). https://doi.org/10.1016/j.ceramint.2017.04.111
35. M. Otoničar, A. Bradeško, S. Salmanov, C.C. Chung, J.L. Jones, T. Rojac, Open Ceram. (2021). https://doi.org/10.1016/j.oceram.2021.100140
36. B. Ameduri, Chem. Rev. **109**, 6632 (2009)
37. P.D. Prasad, J. Hemalatha, J. Magn. Magn. Mater. (2021). https://doi.org/10.1016/j.jmmm.2021.167986
38. A.L. Patterson, Phys. Rev. (1939). https://doi.org/10.1103/PhysRev.56.978
39. C.H. Du, B.K. Zhu, Y.Y. Xu, J. Appl. Polym. Sci. **104**, 2254 (2007)
40. D. Ponnamma, O. Aljarod, H. Parangusan, M. Al Ali Al-Maadeed, Mater. Chem. Phys. (2020). https://doi.org/10.1016/j.matchemphys.2019.122257
41. X. Cai, T. Lei, D. Sun, L. Lin, RSC Adv. **7**, 15382 (2017)
42. R. Gregorio, N. Chaves, P. De, S. Nociti, J. Phys. D. Appl. Phys. (1995). https://doi.org/10.1088/0022-3727/28/2/028
43. L. Li, M. Zhang, M. Rong, W. Ruan, RSC Adv. **4**, 3938 (2014)
44. Y. Peng, P. Wu, Polymer (Guildf) **45**, 5295 (2004)
45. S. Janakiraman, A. Surendran, S. Ghosh, S. Anandhan, A. Venimadhav, Solid State Ion. **292**, 130 (2016)
46. N. Chakhchaoui, R. Farhan, A. Eddiai, M. Meddad, O. Cherkaoui, M. Mazroui, Y. Boughaleb, L. van Langenhove, Mater. Today Proc. **39**, 1148–1152 (2019)
47. S. Yoon, A.A. Prabu, K.J. Kim, C. Park, Macromol. Rapid Commun. **29**, 1316 (2008)
48. P. Zhang, X. Zhao, X. Zhang, Y. Lai, X. Wang, J. Li, G. Wei, Z. Su, ACS Appl. Mater. Interfaces **6**, 7563 (2014)
49. J. Li, Q. Meng, W. Li, Z. Zhang, J. Appl. Polym. Sci. **122**, 1659 (2011)
50. J. Y. Lim, S. Kim, Y. Seo, AIP Conf. Proc. 1–5 (2015)
51. B. Li, X. Wang, K. Li, Y. Wan, S. Zhang, Z. Yang, L. Meng, H. Zou, J. Mater. Sci. Mater. Electron. **31**, 21661 (2020)
52. X.Y. Tong, Y.T. Yang, Z.Z. Du, M.W. Song, J.J. Zhou, H. Liu, C.L. Guan, J. Mater. Sci. Mater. Electron. (2022). https://doi.org/10.1007/s10854-022-08939-7
53. X. Huang, P. Wang, L. Zhang, D. Bi, K. Li, J. Yang, G. Jian, Q. Wang, S. Yu, R. Sun, X. Cao, Z. Fu, J. Mater. Sci. Mater. Electron. (2023). https://doi.org/10.1007/s10854-023-10836-6
54. M.A. Salam, Q.M. Rahman, *Fundamentals of electrical circuit analysis* (Springer, Singapore, 2018), pp.978–981
55. H. Xiao, M. Pan, J.Y.H. Chu, C.R. Bowen, S. Bader, J. Aranda, M. Zhu, Adv. Energy Mater. (2022). https://doi.org/10.1002/aenm.202103185
56. L. Gu, J. Liu, N. Cui, Q. Xu, T. Du, L. Zhang, Z. Wang, C. Long, Y. Qin, Nat. Commun. (2020). https://doi.org/10.1038/s41467-020-14846-4
57. M. Xie, Y. Zhang, M.J. Kraśny, A. Rhead, C. Bowen, M. Arafa, Mech. Syst. Signal Process. **107**, 429 (2018)
58. M. Safaei, H.A. Sodano, S.R. Anton, Smart Mater. Struct. (2019). https://doi.org/10.1088/1361-665X/ab36e4
59. C.W. de Silva, *Sensors for control in encyclopedia of physical science and technology*, 3rd edn. (Academic Press, San Diago, 2003), p.609
60. Y. Li, X. Su, K. Liang, C. Luo, P. Li, J. Hu, G. Li, H. Jiang, K. Wang, Microelectron. Eng. (2021). https://doi.org/10.1016/j.mee.2021.111557
61. S. Mirjalali, R. Bagherzadeh, S. Abrishami, M. Asadnia, S. Huang, A. Michael, S. Peng, C.H. Wang, S. Wu, Macromol. Mater. Eng. (2023). https://doi.org/10.1002/mame.202300009
62. S. Niu, N. Matsuhisa, L. Beker, J. Li, S. Wang, J. Wang, Y. Jiang, X. Yan, Y. Yun, W. Burnett, A.S.Y. Poon, J.B.H. Tok, X. Chen, Z. Bao, Nat. Electron. **2**, 361 (2019)
63. X. Tian, P.M. Lee, Y.J. Tan, T.L.Y. Wu, H. Yao, M. Zhang, Z. Li, K.A. Ng, B.C.K. Tee, J.S. Ho, Nat. Electron. **2**, 243 (2019)
64. Q. Shi, B. Dong, T. He, Z. Sun, J. Zhu, Z. Zhang, C. Lee, InfoMat **2**, 1131 (2020)